electronics

MDPI

Article

Quantum Effects Induced by Defects in Thin-Film Structures: A Hybrid Modeling Approach to Conductance and Transmission Analysis

Mariusz Mączka [1,*], Grzegorz Hałdaś [1], Stanisław Pawłowski [2] and Ewa Korzeniewska [3,*]

[1] Department of Electronics Fundamentals, Faculty of Electrical and Computer Engineering, Rzeszow University of Technology, 35-959 Rzeszow, Poland; ghaldas@prz.edu.pl
[2] Department of Electrodynamics and Electrical Machine Systems, Faculty of Electrical and Computer Engineering, Rzeszow University of Technology, 35-959 Rzeszow, Poland; spawlo@prz.edu.pl
[3] Institute of Electrical Engineering Systems, Lodz University of Technology, Stefanowskiego 18 Street, 90-537 Lodz, Poland
* Correspondence: mmaczka@prz.edu.pl (M.M.); ewa.korzeniewska@p.lodz.pl (E.K.)

Abstract: This study investigated the possibility of quantum effects arising from defects resulting from the use of textronic electroconductive thin films and evaluated their impact on control characteristics. A hybrid model, where the classical approach to determine stationary fields based on the boundary element method was combined with a quantum mechanical approach using nonequilibrium Green's functions, was created. The results of conductance and transmission coefficient simulations for different types of defects in the studied structure and a wide range of temperatures assuming two different control modes are presented. Based on the results, the conditions for the occurrence of quantum effects on the surface of conducting paths containing defects were specified, and their impact on conductance in the quantum mechanical approach was estimated.

Keywords: nonequilibrium Green's functions; boundary element method; textronics structure

check for updates

Citation: Mączka, M.; Hałdaś, G.; Pawłowski, S.; Korzeniewska, E. Quantum Effects Induced by Defects in Thin-Film Structures: A Hybrid Modeling Approach to Conductance and Transmission Analysis. *Electronics* **2024**, *13*, 4230. https://doi.org/10.3390/electronics13214230

Academic Editor: Jianguo Zhu

Received: 2 September 2024
Revised: 18 October 2024
Accepted: 25 October 2024
Published: 29 October 2024

Copyright: © 2024 by the authors. Licensee MDPI, Basel, Switzerland. This article is an open access article distributed under the terms and conditions of the Creative Commons Attribution (CC BY) license (https://creativecommons.org/licenses/by/4.0/).

1. Introduction

Wearable electronics, such as smartphones, sensors and smart clothes, have become essential in our lifetime. The development of thin-film technologies for these devices is crucial for their success [1–3]. Various methods, such as chemical deposition (CVD) [4–8] and physical vacuum deposition (PVD) [9–13], are used to create thin and high-quality layers for wearable electronics. The cleanliness of these layers is important for electronic components. Techniques like magnetron sputtering [14–18] and lithography [19–21] allow for the precise and fast production of thin layers with different thicknesses and structures. These technologies ensure good electrical and thermal conductivity in lightweight and flexible structures for wearable electronics. Thin metal layers can be applied to different substrates, making devices more comfortable and functional. When thin-film structures constituting elements of electronic systems are created on fabric bases, it involves a growing area of research known as textronics.

By utilizing thin electrically conductive layers, it is now feasible to achieve uniform layers of only a few nanometers in thickness, resulting in devices that are extremely slim, durable and efficient.

When thin-film structures are exposed to usage, such as bending and abrasion, they undergo a process where their thickness decreases and defects appear in both the volume and on the surface. They can be observed using microscopy or tomography [22–24]. Among the physical phenomena that occur during the electrical conduction of such structures, the occurrence of quantum effects should be considered. Their understanding and use can be a significant step forward in the design of advanced systems of this type. Even

though modern wearable electronics are not based on the use of quantum phenomena, the miniaturization of devices [25–27] combined with their intensive use can create conditions for the occurrence of such effects. Quantum phenomena generate control characteristics that are fundamentally different from those that can be observed in classical solutions of electronic systems; therefore, it seems to be an important task to estimate the possibility of their occurrence and assess their impact on transport parameters. Among the known and described low-dimensional effects (both experimentally and modeled), the quantum point contact (QPC) [28–31] or tunnelling through a potential barrier [32–37] can be distinguished. There is a high probability that both of these phenomena may occur in a very thin textronic structure containing defects resulting from its use. Defects in the conductive path combined with the effect of its abrasion generate very thin local constrictions reaching sizes in the order of nanometers, which leads to a spatial restriction of electron movement and thus may be the cause of quantum effects.

This work aims to model typical low-dimensional effects resulting from defects that may occur in textronic structures and assess their impact on the conductivity of conductive paths. The idea for the model is based on photographs of surfaces with cracks and defects in conductive paths. The described innovative method of modeling textile structures is unique. Comparable models using similar imaging techniques are available in [38–40]. A numerical model, which is a hybrid of the classical approach to determining stationary fields [41] and the Green function method [42–45] allowing for calculating transport parameters in low-dimensional systems, is proposed in this paper. Simulations of quantum effects consisted of determining the aforementioned transport parameters for typical cases of the occurrence of defects with sizes of fractions of micrometers on very thin areas of conductive paths of textronic structures. The dependence of conductance on the size of these defects for different temperatures and power supply conditions provides an answer to the question of whether we are dealing with quantum conductivity. Additionally, the possibility of quantitative calculation for both cases allows an assessment of the size of the influence of selected effects on the total conductance of the tested structure. The analysis presented in the text, previously unseen in the literature, is important both from the point of view of understanding the phenomena that occur in thin-film structures used in wearable electronics systems and the design of such solutions.

2. Materials and Methods

The authors' earlier works concern, among others, the analysis of current conduction phenomena in electroconductive thin-film layers made on composite textile substrates produced in the PVD process. The technological process of creating such structures is described in [13,46]. Such structures are used in textronics or wearable electronics. Due to their use in sensor systems [47,48], it is important to know the phenomena accompanying the current flow in films of about 200 nm thick.

The present research was carried out on the assumption that as a result of the use of the textronic structure, conductive areas with defects that prevent current conduction appear. This is illustrated in the microscopic photograph in Figure 1a, where the cracks in the conductive surface formed as a result of use can be seen in the form of vertical lines, which are significant obstacles to the classical flow of current in the textronic structure.

This can be seen by analyzing the current density vector field visible in Figure 1b, calculated using the model described previously by the authors of [46]. The very small values of the vector modes (blue and green colors) and their local absence (white areas) testify to the local absence of conditions for classical current flow and raise the legitimate question of whether the quantum nature of the flow of charge carriers occurs in these areas. The same figure shows (see red circles) selected characteristics from the point of view of the research work, namely, constrictions of the conducting surface, which can be the main cause of the previously mentioned white areas in the vector field of current flow. Such obstructions, combined with the limiting thickness of the conductive layers (abrasion effect), can limit the movement of electrons to the size of a fraction of a micrometer, providing

the possibility of producing low-dimensional effects. One such effect is the formation of conduction steps on the control characteristics (see diagram in Figure 1c), which is a typical example of the quantum effect known as QPC. Not only a sharpened (triangular) shape of the energy barriers can achieve the same control effect. It can also be an arbitrarily generated potential that limits the movement of electrons in one spatial dimension to nanometer sizes (assuming a very small thickness of the conducting path relative to the sample size of the surface). Figure 2 illustrates the defect models considered in this work, referring to the cases of conduction path constriction marked with red circles in Figure 1b.

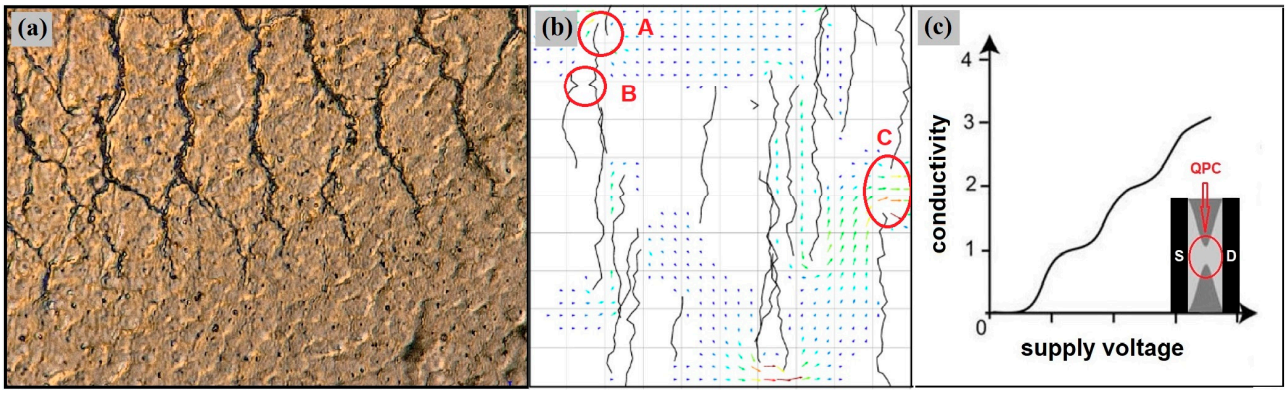

Figure 1. The idea of the quantum effect in the textronic structure: (**a**) cracks in the conducting structure (vertical lines) visible in the photo taken with a microscope; (**b**) simulation of the current density vector field and significant narrowing of the conducting path between defects (red circles) hindering the flow of current (no current vectors) (the results were reprinted from [46]); (**c**) one of the effects of a large narrowing of the conducting surface in the form of a stepped dependence of conductance on the control voltage.

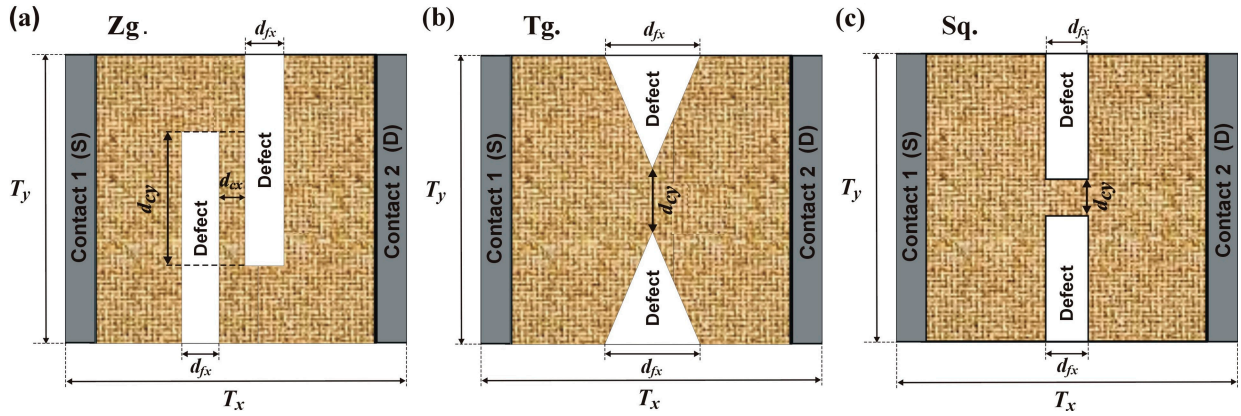

Figure 2. Models of defects present in the studied textronic structure generating constriction referring to the fragments marked with circles in Figure 1b: (**a**) a defect in the form of overlapping rectangular areas and defects in the form of opposite triangles (**b**) and rectangles (**c**).

In addition to the triangular defect, which we have designated as Tg. (see Figure 2b), we also investigated cases of constriction in the form of opposing (designated as Sq.) and overlapping (designated as Zg.) rectangles (see Figures 2c and 2a, respectively).

The numerical model used for the study was based on a combination of the boundary element method used to determine the confinement potential and the Green function method used to calculate the transport parameters. The details are described in the next sections.

2.1. Implementation of the Boundary Element Method

The starting point of the simulation is the determination of the potential distribution on the conductive surface of the textronic structure, for which the classical model shown in Figure 3a–c was used. It allows the calculation of stationary fields in two geometric dimensions and is based on the Boundary Element Method (BEM), which has been widely described in previous works [49–54]. It is assumed that region Ω is filled with a homogeneous isotropic conductor (γ = const.) where no unbalanced electric charges ($\rho = 0$) are present, its surroundings being an ideal dielectric.

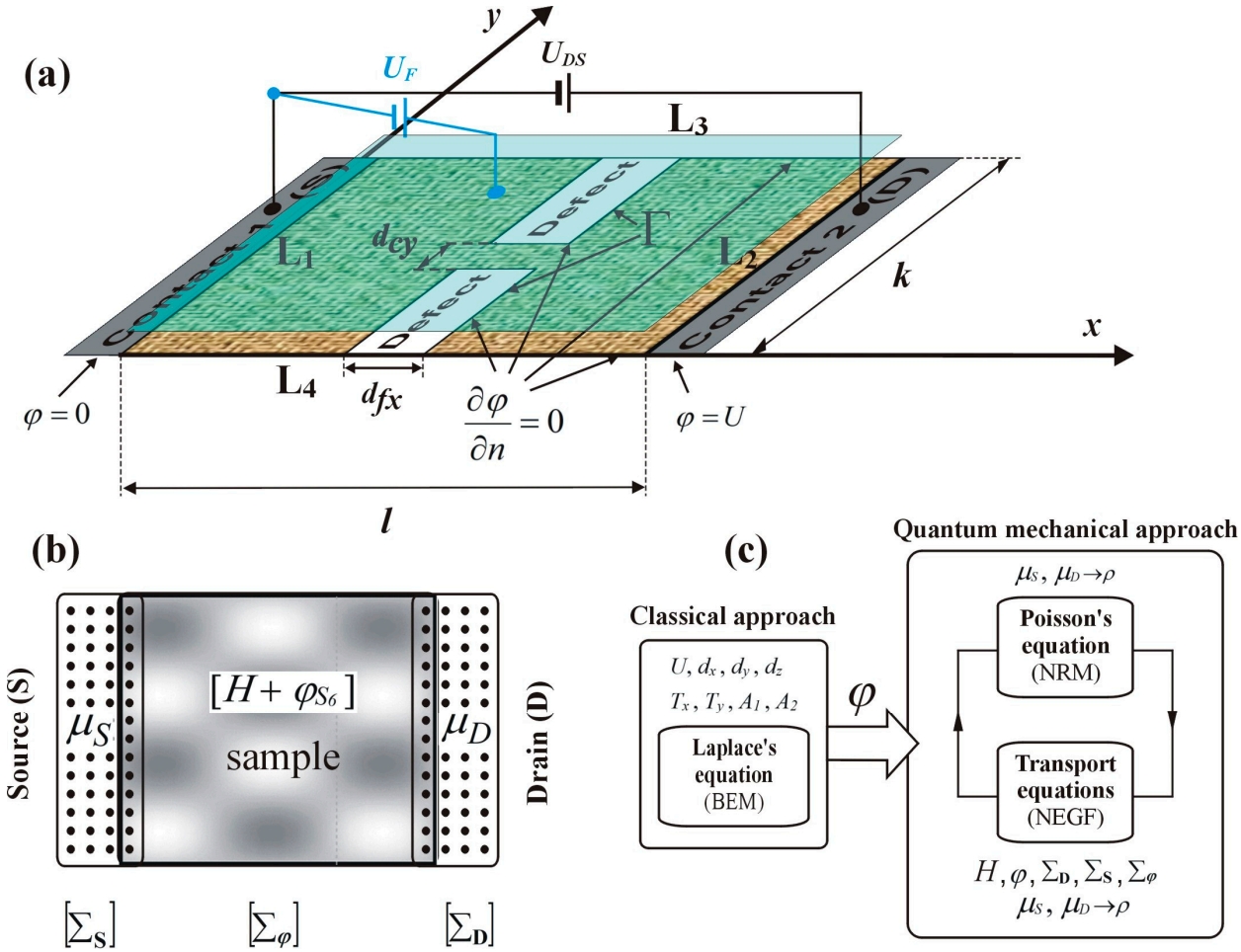

Figure 3. Schematic illustration of the approach to simulating quantum effects in a textronic structure: (**a**) two-dimensional structure model with basic parameters used in the classical approach; (**b**) structure model used in the quantum mechanical approach; (**c**) general scheme for carrying out calculations.

A constant voltage U_{DS} is applied to the contacts labelled Source (S) and Drain (D), which determines the potential difference between the L_1 (φ_S) and L_2 (φ_D) edges of the Ω area. All field functions are independent of the coordinate perpendicular to the surface of the tested conductive area. The above assumptions are forced by the following equation:

$$\vec{E} = -\vec{\text{grad}}\varphi \tag{1}$$

where $\vec{E}$ is the electric field. The potential φ satisfies the Laplace equation:

$$\Delta\varphi = 0 \tag{2}$$

and boundary conditions (Figure 3) in the form

$$\varphi_{L_1} = 0 \tag{3}$$

$$\varphi_{L_2} = U_{DS} \tag{4}$$

$$\left.\frac{\partial \varphi}{\partial n}\right|_{L_3, L_4, \Gamma} = 0 \tag{5}$$

where Γ means the defect boundary on the side of the conducting region. The problem comes down to searching for the solution of Equation (2) with mixed boundary conditions (3)–(5). To solve it, the integral equation method described in works [13,46,50] was used. The numerical application of the above model consists of software modules written in Fortran [55,56] and C++ [57,58] and allows the calculation of the stationary field distribution on a path containing any number of defects of any shape. It was also assumed that the potential in the defect region is equal to the exit energy of the electrons from the material.

2.2. Use of the Nonequilibrium Green Function (NEGF) Method

In the Green's function method, a time-independent Green's function that is a solution of a non-homogeneous differential equation of the form [42] is defined as

$$(z - H)G\left(\mathbf{r}, \mathbf{r}', z\right) = \delta\left(\mathbf{r} - \mathbf{r}'\right) \tag{6}$$

where z is a complex variable with values E = Re{z} and η = Im{z}, H is the Hamiltonian operator and G is the **r** and **r′** function that satisfies the same boundary conditions as the wave function Ψ (r) for the time-independent Schrödinger equation:

$$H(\boldsymbol{r})\Psi(\boldsymbol{r}) = E(\boldsymbol{r})\Psi(\boldsymbol{r}) \tag{7}$$

The application of the Green's function method involves solving the matrix equation in general form:

$$[\mathbf{G}] = (z[\mathbf{I}] - [\mathbf{H}])^{-1} \tag{8}$$

where [**G**] is the Green's function matrix, [**I**] is the unitary matrix and [**H**] is the Hamiltonian matrix. Studying the transport properties of any structure using Green's function method requires attaching semi-infinite electrodes (contacts) to supply the charge, as schematically illustrated in Figure 3b.
Solving the Dyson equation is one step in this approach [59]:

$$\left[\boldsymbol{G}^R\right] = (z[\mathbf{I}] - [\mathbf{H}_{\mathrm{TS}}] - [\boldsymbol{\Sigma}_{\mathrm{D}}] - [\boldsymbol{\Sigma}_{\mathrm{S}}])^{-1} \tag{9}$$

where $\boldsymbol{\Sigma}_{\mathrm{D}}$ and $\boldsymbol{\Sigma}_{\mathrm{S}}$ are self-energy matrices of own leads, $\mathbf{H}_{\mathrm{TS}}$ is the matrix of the Hamiltonian of the structure, while G^R is the matrix of the so-called delayed Green's functions, which can be represented in the form

$$G^R(E) = \lim_{\eta \to 0^+} G(z = E + i\eta) \tag{10}$$

Based on the determined values of the function G^R, it is possible to calculate the local density function of states $\rho(E)$ in i–th node of the studied system, according to the relation:

$$[\boldsymbol{\rho}]_i(E) = -\frac{1}{\pi}\mathrm{Im}\left\{\left[\mathbf{G}^{\mathbf{R}}\right]_{i,j}(E)\right\} \tag{11}$$

The Hamiltonian matrix for the proposed approach is of the form

$$[\mathbf{H}_{\mathrm{TS}}]_{i,j} = \begin{cases} 4t - eV_H(\mathbf{r}_i) - e\phi(\mathbf{r}_i) & \text{for } i = j \\ -t & \text{for n.s.} \\ 0 & \text{for others} \end{cases}, \tag{12}$$

where $\phi(\mathbf{r}_i)$ represents the values of the potential at the nodes of the discretization grid, the abbreviation n.s. means the case when i and j are nearest neighbors, while t is a hopping element whose value is calculated from the expression

$$t \equiv \frac{\hbar^2}{2m^* a^2} \tag{13}$$

where a is the lattice of the model constant and m^* is the effective mass of the electron. The Hartree potential, denoted as $V_H(\mathbf{r}_i)$, is determined from the following relation:

$$V_H(\mathbf{r}_i) = \sum_{j \neq i} \frac{[\mathbf{n}]_j a^2}{|r_{ij}|} + 3.52\,[\mathbf{n}]_i a \tag{14}$$

where $[\mathbf{n}]_i$ is the electron concentration at the i-th node of the system. The conductance between contacts (source—S and drain—D) is determined based on Landauer's formula [60]:

$$g = \frac{2e^2}{h} \sum_{m,n} \int_{-\infty}^{\infty} T_{mn}(E) f(E) dE \tag{15}$$

where $f(E)$ is the Fermi–Dirac function expressing the probability that electrons will occupy energy states, while the T_{mn} transmission coefficient of electrons from channel n in electrode S to channel m in electrode D for energy E, which are calculated using Fisher–Lee formulas [61]:

$$T_{mn} \equiv |[t]_{mn}|^2 \tag{16}$$

$$[t]_{mn} = \mathrm{i}\hbar \sum_{i=1}^{M} \sum_{j=1}^{N} \chi_n(ja) \sqrt{v_n} \left[G^R\right]_{i,j} \chi_m(ia) \sqrt{v_m} \tag{17}$$

where M and N are the numbers of transport modes of the source and drain electrodes, respectively, v_m and v_n are the velocity components in the direction of transport (x) of the waves coming out of the electrodes, while χ_m and χ_n are the transverse components of the wave function of the m-th and n-th modes, respectively, in a specific electrode. As shown in Figure 3c, in the quantum mechanical part of the model, the Poisson equation is also solved using the Newton–Rapson method (NRM) [35]. The numerical implementation of the model described in this chapter consists of several self-written software modules in C++, which are part of the low-dimensional device simulator created by our research group [35,62,63].

3. Results

Numerical studies of quantum effects were carried out for selected shapes of defects of the conducting region illustrated in Figure 2. The most important dimensions of the model and simulation parameters are recorded in Table 1. During the calculations, the total dimensions of the model were assumed to be the same for all types of samples tested ($w_x = w_y = 100$ nm), changing the geometric parameters of individual defects. Initially, the dependence of transmission coefficients (T_{mn}) on energy was analyzed for a conductive path made of silver at different values of polarizing voltages over a wide temperature range, which is also detailed in Table 1.

Table 1. Basic parameters of the model and simulations.

Geometric Dimensions (nm)							Simulation Parameters	
W_x			W_y				material	Ag
100			100				effective mass (kg)	0.96 m_e
Sq.			Zg.		Trg.		temperature (K)	1 ÷ 300
d_{fx}	d_{cy}	d_{fx}	d_{cy}	d_{cx}	d_{fx}	d_{cy}	work function (eV)	4.3
10 ÷ 20	5 ÷ 20	10 ÷ 20	20 ÷ 60	0 ÷ 20	20 ÷ 40	0 ÷ 20	bias voltage (mV)	0 ÷ 300

The most interesting results from this area of research are presented in Figure 4, where selected potential distributions (φ_{2D}) on the surface of a conductive path are plotted for the cases where no defects on the path and defects of the Sq., Zg. and Tg. types are observed. These diagrams reflect the energy barriers encountered by electrons during transport along the surface of a conducting path polarized by voltage $U = U_{DS}$.

Due to the disproportionate height of the aforementioned barriers resulting from the very high value of the electron exit energy from silver (4.3 eV), all graphs in this part of the figure were drawn with a logarithmic scale. The plots in part (f) illustrate the energy dependence of the transmission coefficient T_{mn} for four sizes of Sq.-type defects, which generate the narrowing of the conductive path in the range of 5 to 20 nm in the case of polarization at a voltage value of $U = U_{DS} = 1$ mV. The low-dimensional effect, which is characterized by steps on each of the plotted functions, can be seen. It is also possible to observe the relationship between the size of the constriction (d_{cy}) and the number of steps in the given energy range. The greater the width of the constriction, the more quantum mechanical channels (represented by individual steps in plots) are involved in the conduction process. Another conclusion from the analysis of graph (f) is the fact that the switching moment of the first channel shifts nonlinearly depending on the size of the narrowing and the associated change in the width of the steps (ds). Graph (g) presents the energy dependence of the transmission coefficient T_{mn} for a selected defect size of the Sq. type, producing a conduction path narrowing of width $d_{cy} = 20$ nm. The graphs include control voltages $U = U_{DS} = 1 \div 8$ mV and an energy range of $E = 0 \div 100$ mV.

Analyzing the results obtained in the range shown above, it is possible to observe a practically linear shift in the switching moment of the individual quantum mechanical channels as the control voltage U_{DS} increases, while the regularity of the individual stages disappears. It can cause difficulties in obtaining a quantum effect for the way of controlling the structure described in this paper. The steps become more regular in the situation when, without changing the method of control ($U = U_{DS} = 1 \div 8$ mV), the value of the parameter d_{cy} is reduced (diagrams Figure 4h–i). With this approach, a decreasing range of individual channel shifts from $\Delta s = 26$ meV for $d_{cy} = 20$ nm (Figure 4g) through $\Delta s = 14$ meV for $d_{cy} = 15$ nm (Figure 4h) up to $\Delta s = 11$ meV for $d_{cy} = 10$ nm (Figure 4i) can be observed. On the other hand, very irregular plots of the transmission coefficient are shown in Figure 4j relating to the case of the Zg.-type defect with parameters of $d_{cx} = 20$ nm, $d_{fx} = 20$ nm and $d_{cy} = 60$ nm. However, the outline of the conductance steps can be seen, indicating the activation of the individual. On the other hand, the lack of a clear plateau suggests that the observation of any quantum effect in this case will be very difficult.

The complete absence of charge flow can be seen in Figure 4k where the maximum value of the transmission coefficient is $T_{mn} = 7.2 \cdot 10^{-52}$. The reason is that the conductive path is divided over its entire width by a very high energy barrier ($d_{cx} = 0$ nm), which at the width of $d_{cy} = 60$ nm has a thickness of $2d_{fx}$ and on the rest of the cross-section a thickness of d_{fx}. Subsequent numerical studies have shown that decreasing the width of the d_{fx} barrier increases the values of the transmission coefficient (e.g., $T_{mn} = 1.2 \cdot 10^{-3}$ for $d_{fx} = 1$ nm) many times, but due to its very small values, it does not cause any visible improvement in the aspect of effective conductivity, not to mention obtaining quantum effects.

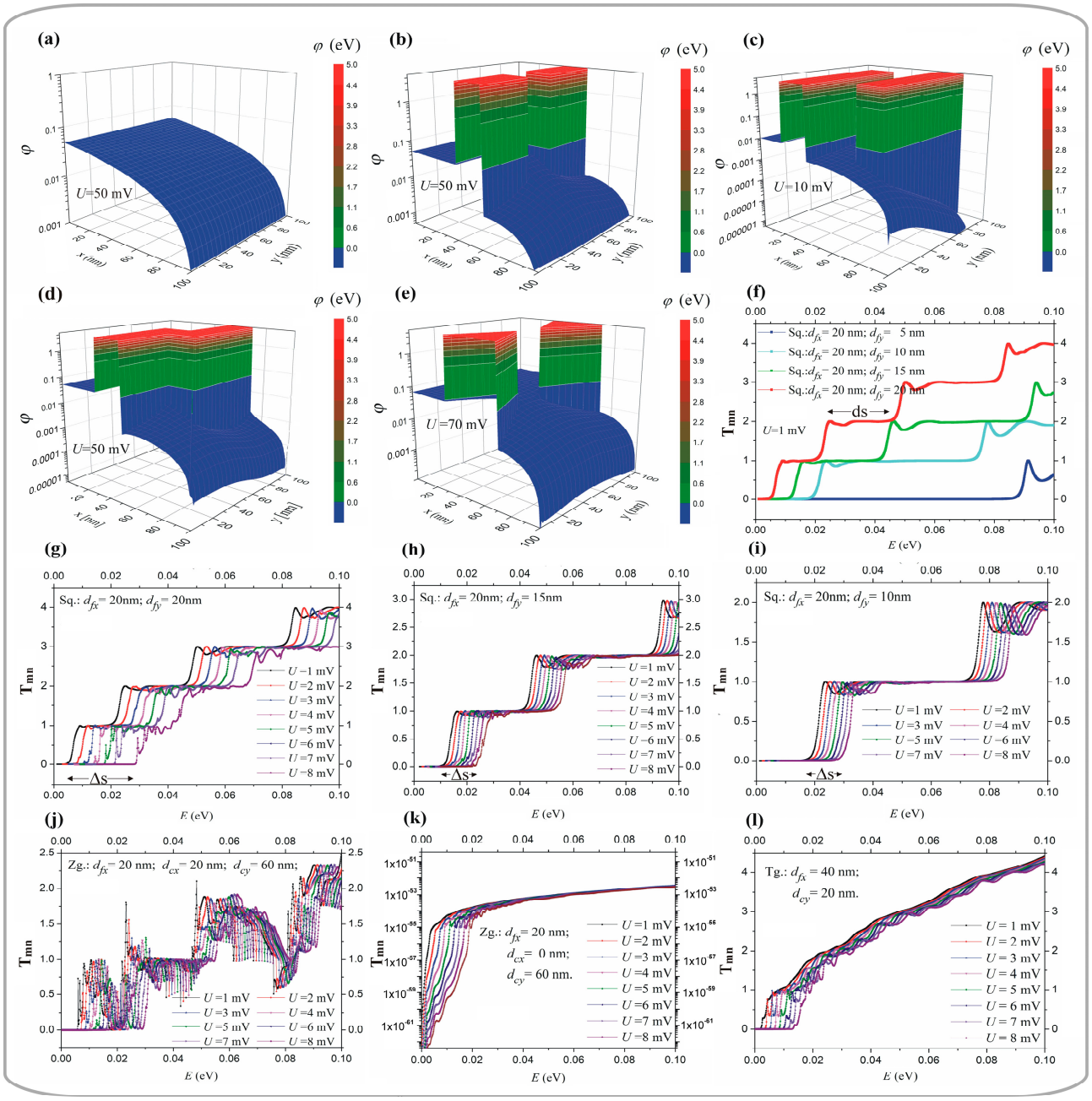

Figure 4. Potential distributions on the surface of the conductive path without defects (**a**) and for defects (**b**–**e**) seen in Figure 2a–c, and the dependence of T_{mn} transmission coefficients on energy (**f**–**l**) for the aforementioned defects.

Slight differences to the character of variation described so far are shown in the T_{mn} (E) functions visible in Figure 4l. They were prepared for a defect of Tg. type with parameters d_{fx} = 40 nm, d_{cy} = 20 nm. The transmission coefficient values in the range of 1 to 4 testify to four more quantum mechanical channels incorporated in the charge transport process at a certain level of controlling the structure with a voltage of $U = U_{DS} = 1 \div 8$ mV. However, the apparent lack of clear steps (plateau) in the individual graphs makes it practically impossible to obtain the quantum effect for this case.

To sum up this part of the study, it can be concluded that the possibility of quantum effects depends not only on the limitation of the size of the conducting path but also to a large extent on the shape of the defect which can be observed in the structure. The greatest

chance of the quantum effect occurring is in the case of limiting the conductive path using Sq.-type barriers, in which the conductive path is narrowed along the transport direction.

However, to make the quantum effect noticeable, in addition to the transmission coefficient considered so far, it is necessary to consider the ambient conditions (temperature) and the way the structure is controlled (supply voltage and position of the Fermi level). The research in this regard consisted of determining the conductance according to relation (10) and the results are illustrated in detail in Figure 5.

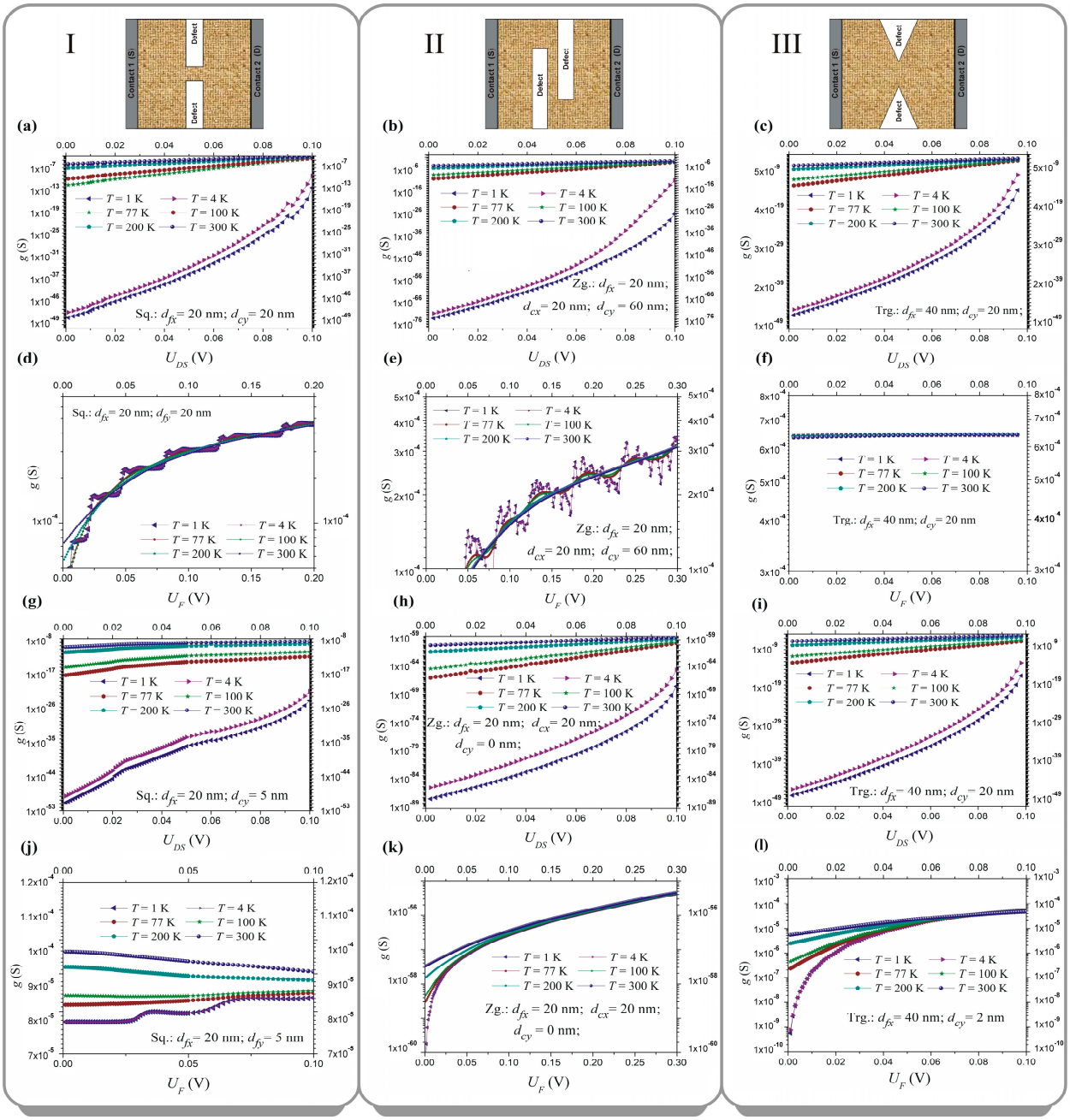

Figure 5. Selected dependencies of conductive path conductance on structure control voltages (U_{DS} and U_F) for the defects shown in Figure 2 and temperatures in the range of 1 ÷ 300 K. For the Sq type defect, graphs (**a**,**d**,**g**,**j**); for the Tg type defect, graphs (**c**,**f**,**i**,**l**); for the Zg type defect, graphs (**b**,**e**,**h**,**k**).

Analyzing the simulation results seen in the first column (I) in Figure 5a, where the conductance dependence of the control voltage U_{DS} is plotted for different temperatures, it

can be concluded that despite favorable preconditions for quantum effects in the case of the Sq.-type defect (Figure 4f–g), they are not observed and classical transport exists.

The situation changes when a different way of controlling the structure is applied. In that case, an additional isolated electrode is connected, which can control the concentration of the flowing charge (Figure 3) in contrast to the case of (a), where the polarization of the structure along the direction of transport is the only phenomenon. When such control is enabled, the graphs seen in part (d) show conductance steps with distinct plateau fragments, which indicate the quantum conduction nature of the structure. However, the success in this case is partial, since the quantum effect is noticeable only for very small values of temperature (T = 1 K and T = 4 K). Similar phenomena were observed while decreasing the width of the conduction path using the d_{cy} parameter and this is exemplified in diagrams (g) and (j)

In the case of the Zg.-type defect, some symptoms of quantum conductance can be seen in graph (f), where, when U_F voltage (at U_{DS} = 2 mV) is used as the means of control, regular steps of conductance can be seen for temperatures T = 77 K and T = 100 K. This contrasts with the large variation in conductance values at very low temperatures (T = 1 K and T = 4 K) and its linear nature of change for high temperatures (T = 200 K and T = 300 K). The other graphs shown in part II in Figure 5 do not show any effects related to conductance quantization, while attention should be paid to graph (k), when the complete blockage of transport by the potential barrier is observed. Both values of the transmission coefficients (Figure 4k) and the directly derived conductance values demonstrate the complete absence of conductivity in the structure. In further experiments, the d_{fx} parameter was decreased to check the threshold for the possible occurrence of resonant tunnelling; however, even for d_{fx} = 1 nm, values of $T_{mn} = 10^{-3}$ were obtained, which is insufficient to enable any quantum mechanical channel.

The graphs in part III of Figure 5 refer to the case of a Tg.-type defect, which makes the structure exhibit no quantum instrument characteristics, regardless of temperature and control method and, with sufficiently distant defects (Figure 5f), the conductance is constant over a relatively wide range of voltages and temperatures.

Determining the effect of the considered types of defects on the conductance in comparison to the conductance of a defect-free conducting surface was one of the aims of this research. The importance of this effect can be estimated by comparing the conductance determined for specific conditions with the data collected in Table 2.

Table 2. Maximum conductance values for the cases shown in Figure 5.

Supply:		U_{DS}			U_F		U_{DS}				U_F	
Figure 5:	**(a)**	**(b)**	**(c)**	**(d)**	**(e)**	**(f)**	**(g)**	**(h)**	**(i)**	**(j)**	**(k)**	**(l)**
T (K)	**Maximum Conductance (S)**											
1	6.1×10^{-13}	6.7×10^{-28}	4.7×10^{-13}	5.8×10^{-4}	3.4×10^{-4}	6.3×10^{-4}	6.6×10^{-23}	2.7×10^{-67}	2.1×10^{-16}	8.4×10^{-5}	3.1×10^{-56}	9.6×10^{-5}
4	6.2×10^{-10}	1.5×10^{-13}	4.6×10^{-9}				1.8×10^{-20}	2.8×10^{-64}	4.3×10^{-13}			
77	2.2×10^{-5}	1.1×10^{-5}	3.1×10^{-5}		3.2×10^{-4}		9.1×10^{-11}	2.1×10^{-59}	$1.5 \times 10{-7}$	8.5×10^{-5}		
100	3.1×10^{-5}	1.4×10^{-5}	3.9×10^{-5}				2.1×10^{-9}	3.5×10^{-59}	3.3×10^{-7}			
200	5.4×10^{-5}	2.5×10^{-5}	6.4×10^{-5}		3.1×10^{-4}		3.5×10^{-7}	1.3×10^{-58}	2.1×10^{-6}	9.1×10^{-5}		
300	7.3×10^{-5}	3.4×10^{-13}	8.4×10^{-5}				2.3×10^{-6}	3.1×10^{-58}	4.8×10^{-6}	7.7×10^{-5}		

The maximum conductance values for all the dependencies illustrated in Figure 5 are presented in Table 2. It can be concluded that the U_{DS} voltage control changes the maximum conductance of the tested structure over a very wide range and is strongly

dependent on temperature, while structure controlling with an isolated gate (U_F voltage) keeps the maximum conductance at levels in the order of $10^{-4} \div 10^{-3}$ Siemens. For comparison, the conductance of a conductive path containing no defects was calculated using a quantum mechanical approach, and for an assumed temperature of 300 K and a voltage of U_{DS} = 100 mV, a result of 3.9 S was obtained. The appearance of any defect on a conductive path with very small geometrical dimensions reduces the conductance of the structure 1000–10,000 times.

4. Conclusions

Numerical studies have shown that, in very thin textronic structures of a small size containing defects caused by use (bending, abrasion), it is possible to occur conductance quantization effects but only at very low temperatures (up to 4 K) and for cases when defects generate constrictions along the direction of transport. Furthermore, to achieve quantum control characteristics, an additional isolated electrode must be added to control the concentration of electron gas in the conductive path. From a practical point of view, therefore, the occurrence of a typical quantum effect in PVD structures is unlikely. Nevertheless, where microcracks create constrictions that limit the conduction path to nanometer sizes, the conductivity decreases by several orders of magnitude, irrespective of the type of defect that caused them.

This research has proved to be very important, as it has not only verified assumptions about the possibility of quantum effects on microcracks in PVD structures, but has also indicated the direction in which new solutions should be designed to control such effects. On this basis, it is planned to develop PVD structures in the form of microtransistors, where design simulations based on the model created can significantly speed up and optimize the cost of the work.

Author Contributions: Conceptualisation: E.K. and M.M.; methodology: M.M., G.H.and S.P.; software: M.M. and G.H.; validation: M.M. and E.K; formal analysis, S.P., M.M. and E.K. investigation: G.H. and M.M.; resources, G.H. and M.M.; writing—original draft preparation: M.M.; writing—review and editing, M.M. and E.K. All authors have read and agreed to the published version of the manuscript.

Funding: This research received no external funding.

Data Availability Statement: The datasets presented in this article are not readily available because the data are part of an ongoing study or due to technical/time limitations. Requests to access the datasets should be directed to mmaczka@prz.edu.pl.

Conflicts of Interest: The authors declare that they have no known competing financial interest or personal relationships that could have appeared to influence the work reported in this paper.

References

1. Wu, Y.; Mechael, S.; Carmichael, T. Wearable E-Textiles Using a Textile-Centric Design Approach. *Acc. Chem. Res.* **2021**, *54*, 4051–4064. [CrossRef] [PubMed]
2. Choudhry, N.; Arnold, L.; Rasheed, A.; Khan, I.; Wang, L. Textronics—A Review of Textile-Based Wearable Electronics. *Adv. Eng. Mater.* **2021**, *23*, 2100469. [CrossRef]
3. Stoppa, M.; Chiolerio, A. Wearable Electronics and Smart Textiles: A Critical Review. *Sensors* **2014**, *14*, 11957–11992. [CrossRef] [PubMed]
4. Hong, H.C.; Ryu, J.I.; Lee, H.C. Recent Understanding in the Chemical Vapor Deposition of Multilayer Graphene: Controlling Uniformity, Thickness, and Stacking Configuration. *Nanomaterials* **2023**, *13*, 2217. [CrossRef] [PubMed]
5. Choy, K. Chemical vapour deposition of coatings. *Prog. Mater. Sci.* **2003**, *48*, 57–170. [CrossRef]
6. Asatekin, A.; Barr, M.; Baxamusa, S.; Lau, K.; Tenhaeff, W.; Xu, J.; Gleason, K. Designing polymer surfaces via vapor deposition. *Mater. Today* **2010**, *13*, 26–33. [CrossRef]
7. Billard, A.; Maury, F.; Aubry, P.; Balbaud-Célérier, F.; Bernard, B.; Lomello, F.; Maskrot, H.; Meillot, E.; Michau, A.; Schuster, F. Emerging processes for metallurgical coatings and thin films. *Comptes Rendus Phys.* **2018**, *19*, 755–768. [CrossRef]
8. Butt, M.A. Thin-Film Coating Methods: A Successful Marriage of High-Quality and Cost-Effectiveness—A Brief Exploration. *Coatings* **2022**, *12*, 1115. [CrossRef]

9. Baptista, A.; Silva, F.; Porteiro, J.; Míguez, J.; Pinto, G. Sputtering Physical Vapour Deposition (PVD) Coatings: A Critical Review on Process Improvement and Market Trend Demands. *Coatings* **2018**, *8*, 402. [CrossRef]
10. Gudmundsson, J.; Anders, A.; Keudell, A. Foundations of physical vapor deposition with plasma assistance. *Plasma Sources Sci. Technol.* **2022**, *31*, 083001. [CrossRef]
11. Ferreira, A.; Silva, F.; Pinto, A.; Sousa, V. Characterization of Thin Chromium Coatings Produced by PVD Sputtering for Optical Applications. *Coatings* **2021**, *11*, 215. [CrossRef]
12. Aliofkhazraei, M.; Ali, N. PVD Technology in Fabrication of Micro- and Nanostructured Coatings. *Compr. Mater. Process.* **2014**, *7*, 49–84. [CrossRef]
13. Pawłowski, S.; Plewako, J.; Korzeniewska, E. Analysis of flow field distribution in a thin conductive layer with an elliptical defect. *Prz. Elektrotechniczny* **2020**, *96*, 234–237. [CrossRef]
14. Padamata, S.; Yasinskiy, A.; Yanov, V.; Saevarsdottir, G. Magnetron Sputtering High-Entropy Alloy Coatings: A Mini-Review. *Metals* **2022**, *12*, 319. [CrossRef]
15. Palmero, A.; Martin, N. Advanced Strategies in Thin Film Engineering by Magnetron Sputtering. *Coatings* **2020**, *10*, 419. [CrossRef]
16. Huang, M.; Wu, Y.; Yi, N.; Lu, S. Structural colouration on textile fabrics with thin-film coating via magnetron sputtering: A review. *Surf. Eng.* **2022**, *38*, 830–845. [CrossRef]
17. Bräuer, G.; Szyszka, B.; Vergöhl, M.; Bandorf, R. Magnetron sputtering–Milestones of 30 years. *Vacuum* **2010**, *84*, 1354–1359. [CrossRef]
18. Miśkiewicz, P.; Tokarska, M.; Frydrych, I.; Makówka, M. Evaluation of Thermal Properties of Certain Flame-Retardant Fabrics Modified with a Magnetron Sputtering Method. *Autex Res. J.* **2020**, *20*, 168–177. [CrossRef]
19. Tahir, U.; Kamran, M.; Jang, M.; Jeong, M. Thin-film coating on cylinder for fabrication of cylindrical mold: Roll-to-roll nano-imprint lithography. *Microelectron. Eng.* **2019**, *211*, 5–12. [CrossRef]
20. Chou, S.; Krauss, P.; Renstrom, P. Imprint Lithography with 25-Nanometer Resolution. *Science* **1996**, *272*, 85–87. [CrossRef]
21. Suh, K.; Lee, H. Capillary Force Lithography: Large-Area Patterning, Self-Organization, and Anisotropic Dewetting. *Adv. Funct. Mater.* **2002**, *12*, 405–413. [CrossRef]
22. Rymarczyk, T.; Nita, P.; Vejar, A.; Wos, M.; Stefaniak, B.; Adamkiewicz, P. Wareable mobile measuring device based on electrical tomography. *Prz. Elektrotechniczny* **2019**, *95*, 211–214. [CrossRef]
23. Rymarczyk, T.; Klosowski, G.; Tchorzewski, P.; Cieplak, T.; Kozlowski, E. Area monitoring using the ERT method with multisensor electrodes. *Prz. Elektrotechniczny* **2019**, *95*, 153–156. [CrossRef]
24. Gocławski, J.; Korzeniewska, E.; Sekulska-Nalewajko, J.; Sankowski, D.; Pawlak, R. Extraction of the Polyurethane Layer in Textile Composites for Textronics Applications Using Optical Coherence Tomography. *Polymers* **2018**, *10*, 469. [CrossRef]
25. Maheshwari, N.; Abd-Ellah, M.; Goldthorpe, I.A. Transfer printing of silver nanowire conductive ink for e-textile applications. *Flex. Print. Electron.* **2019**, *4*, 025005. [CrossRef]
26. He, T.; Shi, Q.; Wang, H.; Wen, F.; Chen, T. Nano Energy Beyond energy harvesting-multi-functional triboelectric nanosensors on a textile. *Nano Energy* **2019**, *57*, 338–352. [CrossRef]
27. Tseghai, G.B.; Malengier, B.; Fante, K.A.; Nigusse, A.B.; Van Langenhove, L. Integration of Conductive Materials with Textile Structures, an Overview. *Sensors* **2020**, *20*, 6910. [CrossRef]
28. Berggren, K.-F.; Pepper, M. Electrons in one dimension. *Philos. Trans. R. Soc. A* **2010**, *368*, 1141–1162. [CrossRef]
29. Lassl, A.; Schlagheck, P.; Richter, K. Effects of short-range interactions on transport through quantum point contacts: A numerical approach. *Phys. Rev. B* **2007**, *75*, 045346. [CrossRef]
30. Maao, F.A.; Zozulenko, I.V.; Hauge, E.H. Quantum point contacts with smooth geometries: Exact versus approximate results. *Phys. Rev. B* **1994**, *50*, 17320. [CrossRef]
31. Davies, J.H. *The Physics of Low-Dimensional Semiconductors*; Cambridge University Press: Cambridge, UK, 1998.
32. Sheela, L.; Balamurugan, N.B.; Balamurugan, N.B.; Sudha, S.; Jasmine, J. Analysis of Tunnelling Rate Effect on Single Electron Transistor. *J. Electr. Eng. Technol.* **2014**, *9*, 1670–1676. [CrossRef]
33. Schiff, L.I. *Quantum Mechanics*; McGraw-Hill: New York, NY, USA, 1968.
34. Shashurin, V.D.; Vetrova, N.A.; Filyaev, A.A. Evaluation of channel transmission of nanoelectronic devices on low-dimensional structures with quantum confinement. *J. Phys. Conf. Ser.* **2020**, *1560*, 012048. [CrossRef]
35. Mączka, M. Effective Simulations of Electronic Transport in 2D Structures Based on Semiconductor Superlattice Infinite Model. *Electronics* **2020**, *9*, 1845. [CrossRef]
36. Datta, S. *Electronic Transport in Mesoscopic Systems*; Cambridge University Press: Cambridge, UK, 1995.
37. Ehrenreich, H.; Turnbull, D. *Solid State Physics: Advances in Research and Applications*; Academic Press Inc.: Boston, MA, USA, 1991; Volume 44.
38. Connolly, M.R.; Puddy, R.K.; Logoteta, D.; Marconcini, P.; Roy, M.; Griffiths, J.P.; Smith, C.G. Unraveling Quantum Hall Breakdown in Bilayer Graphene with Scanning Gate Microscopy. *Nano Lett.* **2012**, *12*, 5448–5454. [CrossRef] [PubMed]
39. Baumgartner, A.; Ihn, T.; Ensslin, K.; Maranowski, K.; Gossard, A.C. Quantum Hall effect transition in scanning gate experiments. *Phys. Rev. B* **2007**, *76*, 085316. [CrossRef]
40. Kičin, S.; Pioda, A.; Ihn, T.; Ensslin, K.; Driscoll, D.C.; Gossard, A.C. Local backscattering in the quantum Hall regime. *Phys. Rev. B* **2004**, *70*, 205302. [CrossRef]

41. Pawłowski, S.; Plewako, J.; Korzeniewska, E. Field modelling the impact of cracks on the electroconductivity of thin-film textronic structures. *Electronics* **2020**, *9*, 402. [CrossRef]
42. Datta, S. The non-equilibrium Green's function (NEGF) formalism: An elementary introduction. In *Digest. International Electron Devices Meeting, San Francisco, CA, USA*; IEEE: Piscataway, NJ, USA, 2002; pp. 703–706. [CrossRef]
43. Pan, E. Static Green's functions in multilayered half spaces. *Appl. Math. Model.* **1997**, *21*, 509–521. [CrossRef]
44. Chen, Y.; Chew, W.; Jiang, L. A New Green's Function Formulation for Modeling Homogeneous Objects in Layered Medium. *IEEE Trans. Antennas Propag.* **2012**, *60*, 4766–4776. [CrossRef]
45. Bruno, O.; Lyon, M.; Pérez-Arancibia, C.; Turc, C. Windowed Green Function Method for Layered-Media Scattering. *SIAM J. Appl. Math.* **2015**, *76*, 1871–1898. [CrossRef]
46. Pawłowski, S.; Plewako, J.; Korzeniewska, E. Field Modeling of the Influence of Defects Caused by Bending of Conductive Textronic Layers on Their Electrical Conductivity. *Sensors* **2023**, *23*, 1487. [CrossRef] [PubMed]
47. Korzeniewska, E.; Krawczyk, A.; Mróz, J.; Wyszyńska, E.; Zawiślak, R. Applications of Smart Textiles in Post-Stroke Rehabilitation. *Sensors* **2020**, *20*, 2370. [CrossRef]
48. Korzeniewska, E.; Szczęsny, A.; Lipiński, P.; Dróżdż, T.; Kiełbasa, P.; Miernik, A. Prototype of a Textronic Sensor Created with a Physical Vacuum Deposition Process for Staphylococcus aureus Detection. *Sensors* **2021**, *21*, 183. [CrossRef]
49. Brebbia, C.A. *Boundary Element Methods in Engineering*; Springer: Berlin/Heidelberg, Germany, 1978.
50. Jaswon, M.A. Integral equation methods in potential theory. I. *Proc. R. Soc. Lond.* **1963**, *275*, 23–32. [CrossRef]
51. Xu, S.; Niu, H.; Su, M. Electrostatic Simulation in 2D with the Boundary Element Method. *IEEE Trans. Magn.* **2022**, *58*, 3203405. [CrossRef]
52. Liu, B.; Zhang, H.; Li, J. Accurate Field Computation with the Boundary Element Method. *J. Mech. Mater. Struct.* **2020**, *15*, 453–467. [CrossRef]
53. Liang, X.; Wang, L. The Boundary Element Method for Ordinary State-Based Peridynamics. *Comput. Model. Eng. Sci.* **2024**, *139*, 2807–2834. [CrossRef]
54. Reutskiy, S.Y. The Method of Approximate Fundamental Solutions for Axisymmetric Problems with Laplace Operator. *Eng. Anal. Bound. Elem.* **2023**, *31*, 410–415. [CrossRef]
55. Metcalf, M.; Reid, J.; Cohen, M. *Modern Fortran Explained*; Oxford Scholarship Online: Oxford, UK, 2011. [CrossRef]
56. Akin, J.; Singh, M. Object-oriented Fortran 90 P-adaptive finite element method. *Adv. Eng. Softw.* **2000**, *33*, 461–468. [CrossRef]
57. Stroustrup, B. *Foundations of C++*; Springer Nature link: Berlin/Heidelberg, Germany, 2012; pp. 1–25. [CrossRef]
58. Bergmann, S. *Computer Science Principles with C++*; Rowan Digital Works: Glassboro, NJ, USA, 2021. [CrossRef]
59. Dyson, F. The S Matrix in Quantum Electrodynamics. *Phys. Rev.* **1949**, *75*, 1736. [CrossRef]
60. Landauer, R. Conductance from transmission: Common sense points. *Phys. Scr.* **1992**, *1992*, 110. [CrossRef]
61. Fisher, D.S.; Lee, P.A. Relation between conductivity and transmission matrix. *Phys. Rev. B* **1981**, *23*, 6851. [CrossRef]
62. Mączka, M.; Hałdaś, G. Three dimensional simulator of the single electron transistor based on ISIS structure. *Phys. E Low-Dimens. Syst. Nanostruct.* **2012**, *44*, 1202–1208; ISSN 1386-9477. [CrossRef]
63. Hałdaś, G.; Mączka, M. Quantum point contact simulations on ISIS structure. *Electron. Technol. Internet J.* **2006**, *37*, 1–6.

Disclaimer/Publisher's Note: The statements, opinions and data contained in all publications are solely those of the individual author(s) and contributor(s) and not of MDPI and/or the editor(s). MDPI and/or the editor(s) disclaim responsibility for any injury to people or property resulting from any ideas, methods, instructions or products referred to in the content.